


# SCIENTIFIC REPORTS



OPEN

## Structure and solvents effects on the optical properties of sugar-derived carbon nanodots

Nikolaos Papaioannou<sup>1,2</sup>, Adam Marinovic<sup>3</sup>, Noriko Yoshizawa<sup>4</sup>, Angela E. Goode<sup>5</sup>, Michael Fay<sup>6</sup>, Andrei Khlobystov<sup>6,7</sup>, Maria-Magdalena Titirici<sup>2,3</sup>  & Andrei Sapelkin<sup>1,2</sup>

Carbon nanodots are a new and intriguing class of fluorescent carbon nanomaterials and are considered a promising low cost, nontoxic alternative to traditional inorganic quantum dots in applications such as bioimaging, solar cells, photocatalysis, sensors and others. Despite the abundant available literature, a clear formation mechanism for carbon nanodots prepared hydrothermally from biomass precursors along with the origins of the light emission are still under debate. In this paper, we investigate the relationships between the chemical structure and optical properties of carbon nanodots prepared by the hydrothermal treatment of glucose. Our major finding is that the widely reported excitation-dependent emission originates from solvents used to suspend the as-prepared carbon nanodots, while emission from dry samples shows no excitation-dependence. Another important highlight is that the hydrothermal conversion of biomass-derivatives under subcritical conditions leads to a heterogeneous mixture of amorphous-like nanoparticles, carbon onion-type and crystalline carbons composed of at least three different phases. The potential chemical reaction pathways involved in the formation of these hydrothermal carbon products along with a comprehensive structural and optical characterization of these systems is also provided.

Carbon nanodots (CNDs) represent a new family of carbon nanomaterials. The term refers to nanoscale (usually around or below 10 nm in diameter) particles consisting of mostly carbon atoms and exhibiting photoluminescence (PL) without necessarily showing evidence of quantum effects<sup>1</sup>. CNDs are promising candidates to replace the toxic metal-based semiconductor quantum dots (e.g. CdS, CdSe, CdTe, PbS, etc.) in applications such as bioimaging<sup>2–4</sup>, sensitizers for solar cells<sup>5</sup>, multicolour patterning<sup>6–8</sup> and ions detection<sup>9–11</sup>. Advantages of CNDs over classical semiconductor quantum dots (QDs) include low cytotoxicity, chemical inertness, excellent biocompatibility, tunable surface functionalities, versatile and simple synthesis routes.

CNDs synthesis is divided in two main approaches, including top-down (cutting from different pre-formed carbon structures)<sup>12–14</sup> as well as bottom-up (starting with molecular precursors)<sup>3,15,16</sup> methods that yield a diverse array of CNDs. Hydrothermal carbonization (HTC) of biomass-derivatives has been proposed by Titirici *et al.* as an alternative route to produce carbon materials under milder conditions<sup>17</sup>. Recently this has been adopted for the production of CNDs whereby the CNDs represent the nucleation clusters, which are formed before the growth into the final HTC nanostructured carbon material<sup>12,18,19</sup>. Significant research efforts have been carried out to elucidate the origins of light emission in these materials. The optical properties of hydrothermal carbon nanodots are complex compared to classical organic fluorophores as well as semiconductor quantum dots. They are highly dependent on the carbon dots structural features. Some reports attribute the photoluminescence (PL) in CNDs to band gap transitions of conjugated  $\pi$ -domains within a small crystalline core<sup>20,21</sup>, while others correlate emission to surface-localized states<sup>22,23</sup>. The most reported PL characteristic in hydrothermal CNDs is excitation-dependent emission, while the origin of this phenomenon remains under

<sup>1</sup>School of Physics and Astronomy, Queen Mary, University of London, 327 Mile End Road, London, E1 4NS, UK.

<sup>2</sup>Materials Research Institute, Queen Mary University of London, Mile End Road, E14NS, London, UK. <sup>3</sup>School of Engineering and Materials Science, Queen Mary University of London, Mile End Road, E1 4NS, London, UK.

<sup>4</sup>Electron Microscope Facility, TIA, AIST, 16-1 Onogawa, Tsukuba, 305-8569, Japan. <sup>5</sup>Department of Materials, Faculty of Engineering, Imperial College London, London, SW7 2AZ, UK. <sup>6</sup>Nanoscale and Microscale Research Centre, University of Nottingham, University Park, NG7 2RD, Nottingham, UK. <sup>7</sup>School of Chemistry, University of Nottingham, University Park, Nottingham, NG7 2RD, UK.

Correspondence and requests for materials should be addressed to M.-M.T. (email: [m.m.titirici@qmul.ac.uk](mailto:m.m.titirici@qmul.ac.uk)) or A.S. (email: [a.sapelkin@qmul.ac.uk](mailto:a.sapelkin@qmul.ac.uk))

debate<sup>24</sup>. Even though a number of reports link excitation-dependent emission to the presence of various surface chromophores or quantum confinements due to size differences<sup>25,26</sup>, yet clear evidence is still missing. Recent publications suggest that emission in CNDs changes in different solvents. For example, Wu *et al.* reported that fluorescence emission in their CNDs synthesized via one-step pyrolytic route changed from 400 to 430 nm when suspended in different solvents under the same excitation wavelength<sup>27</sup>. Lin *et al.* indicated that CNDs synthesized from *m*-phenylenediamine showed strong solvent-dependent emission between 400–500 nm<sup>28</sup>. Sciortino and co-workers found a dependence of the emission energy and decay kinetics on solvent properties, which highlights the crucial role of surface moieties<sup>29</sup>. Reckmeier *et al.* showed that emission of edge and surface bands undergoes opposite solvatochromic shifts when solvent polarity is changed<sup>30</sup>. This phenomenon is very similar to the solvatochromism in organic dyes, which is usually attributed to the intramolecular charge transfer but is rarely reported in CNDs<sup>31,32</sup>. None of these reports has actually investigated the differences in PL between the particles in dry state and in solvents with different polarities. Furthermore, there has not been a clear correlation between PL and physicochemical features of CNDs (i.e. functional groups, crystallinity). A typical issue CNDs face in their solid state is very weak fluorescence due to the direct  $\pi$ - $\pi$  interactions similar to organic molecules, which is caused by an excessive resonance energy transfer observed in dry state<sup>33</sup>. To overcome this, Chen and co-workers prepared CNDs and by controlling their surface or interparticle spacing obtained successfully for first time solid-state fluorescence (SSF)<sup>34</sup>.

Literature reports on the formation mechanism of hydrothermal CNDs are scarce. Hu *et al.* proposed a formation mechanism of CNDs prepared from citric acid and monoethanolamine including polymerization, aromatization, nucleation and growth. Initially, monoethanolamine reacts with citric acid through dehydration and polymer nanoparticles with large diameter are formed. Upon heating, the polymer nanoparticles shrink due to continuous dehydration and C=C and C=N bonds are formed. In parallel, aromatic clusters are formed inside the nanoparticles and when their concentration reaches the critical supersaturation point, nucleation of carbon dots takes place. Further nuclei are formed by enhanced aromatization of the polymers and over time carbon dots increase in both number and size. Finally, the polymers disappear and carbon dots remain<sup>35</sup>. Similar approach was reported by De *et al.* for the formation of their CNDs under pyrolysis<sup>36</sup>. Similarly, Sun *et al.*, reported the formation mechanism of CD from citric acid and urea under hydrothermal conditions, which promote formation of amide between -NH<sub>2</sub> and -COOH followed by intramolecular hydrolysis between neighbour amide and COOH groups leading to formation of pyrrolic N within the carbon framework<sup>37</sup>. Xiao *et al.* used a polymer (PEG400) in presence of NaOH for the synthesis of CNDs. Reaction occurred when the carbon source pyrolyzed and oxidized in the alkaline environment which resulted in the formation of small particles that progressively aggregated to form clusters and finally the CNDs<sup>38</sup>.

Hydrothermal carbonization of biomass derivatives such as glucose utilized here is a complex process. Our group has previously studied the formation mechanism of amorphous carbon microspheres from glucose forming via a nucleation-polymerization process. (See Supplementary Information, Scheme S1)<sup>39</sup>.

Herein, we examine the relationship between structural and optical properties in CNDs prepared by HTC from glucose selected as a model system and examine their PL in different environments including the dry state to examine thoroughly the solvatochromic phenomenon. Furthermore, we propose a mechanism of formation of CNDs during HTC synthesis process.

## Results and Discussion

CNDs were prepared via hydrothermal carbonization (HTC) of glucose by simply treating a 4% w/v aqueous glucose solution at 200 °C for 6 hours followed by centrifugation and filtration to isolate the CNDs from the larger micrometer sized carbon particles. As-prepared CNDs appear as yellow aqueous suspension that shows strong blue emission when illuminated by UV light (see Fig. S1). This is in good agreement with previous reports where many other carbon-based precursors were used<sup>40–43</sup>. Further, the glucose-derived CNDs solution was freeze dried to obtain a powdered form of the product. Initially, we investigated the morphology of the resulting glucose-derived CNDs from aqueous suspension using transmission electron microscopy (TEM) at 200 kV. (Fig. 1a,b).

The TEM images show crystalline CNDs where clear lattice fringes are observed which are surrounded by an amorphous carbon matrix. The electron diffraction patterns (Fig. 1c) confirm the crystallinity of our glucose-derived CNDs showing lattice fringes spaced around 0.32 nm, which is close to the graphite (002) (0.3354 nm). The size of the carbon nanodots was measured from TEM images using ImageJ software, and histograms of the size distributions are shown in Fig. 1d from which the average size and standard deviation was calculated. Based on the statistics of about 120 particles in several TEM images, size distribution measurements show that the average diameter of the as synthesized glucose carbon nanodots is  $(5.15 \pm 0.83)$  nm.

Our XRD and Raman data recorded on freeze-dried CNDs (Fig. 2) do not fully support the presence of crystalline nanoparticles. The XRD pattern shown in Fig. 2a shows a single broad peak at around 22.5° again indicating a significant level of topological disorder in the sample. The 002 peak at about  $2\theta = 22.5^\circ$  corresponds to a set of sp<sup>2</sup> carbons-graphitic carbons with stacking faults, known as turbostratic carbons. No other peaks are detected in XRD suggesting amorphous nature of our materials.

Raman data are shown in Fig. 2b, while the results from Raman analysis are summarized in Table 1. We clearly observe two of the main Raman peaks normally found in low dimensional carbon systems (e.g. carbon nanotubes, graphene, graphene oxide, carbon black): D and G bands around 1330 cm<sup>-1</sup> and 1590 cm<sup>-1</sup> respectively. Note that D band is not observed in perfect crystalline graphite nor graphene and it is usually associated with some form of lattice disorder (e.g. impurities, cluster size effects, presence of sp<sup>3</sup> bonds etc.<sup>44</sup>). Combinations of Lorentzian, Gaussian and Breit-Wigner-Fano (BWF) peaks are normally used to extract numerical information<sup>45</sup>. Considering that G band in all samples is clearly asymmetric we used Lorentzian peak shape to fit D band and

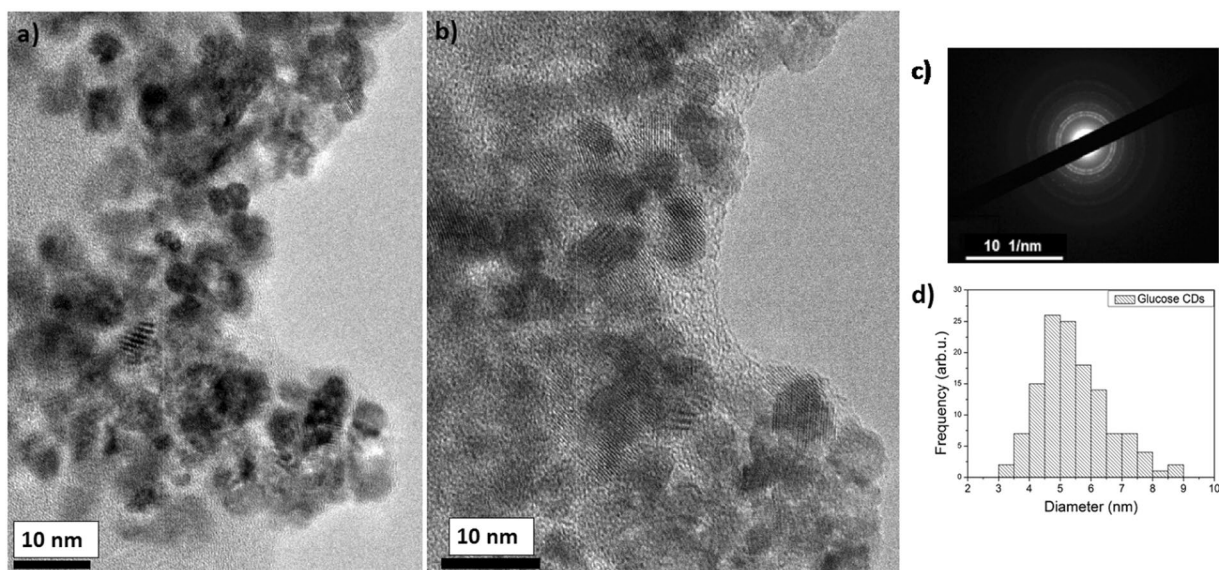


**Figure 1.** (a and b) TEM of glucose derived CNDs taken at 200 kV showing crystalline nanoparticles, with diameters below 10 nm, surrounded by an amorphous carbon matrix; (c) electron diffraction pattern of (a and b,c) average particle size distribution of the particles in (a and b).

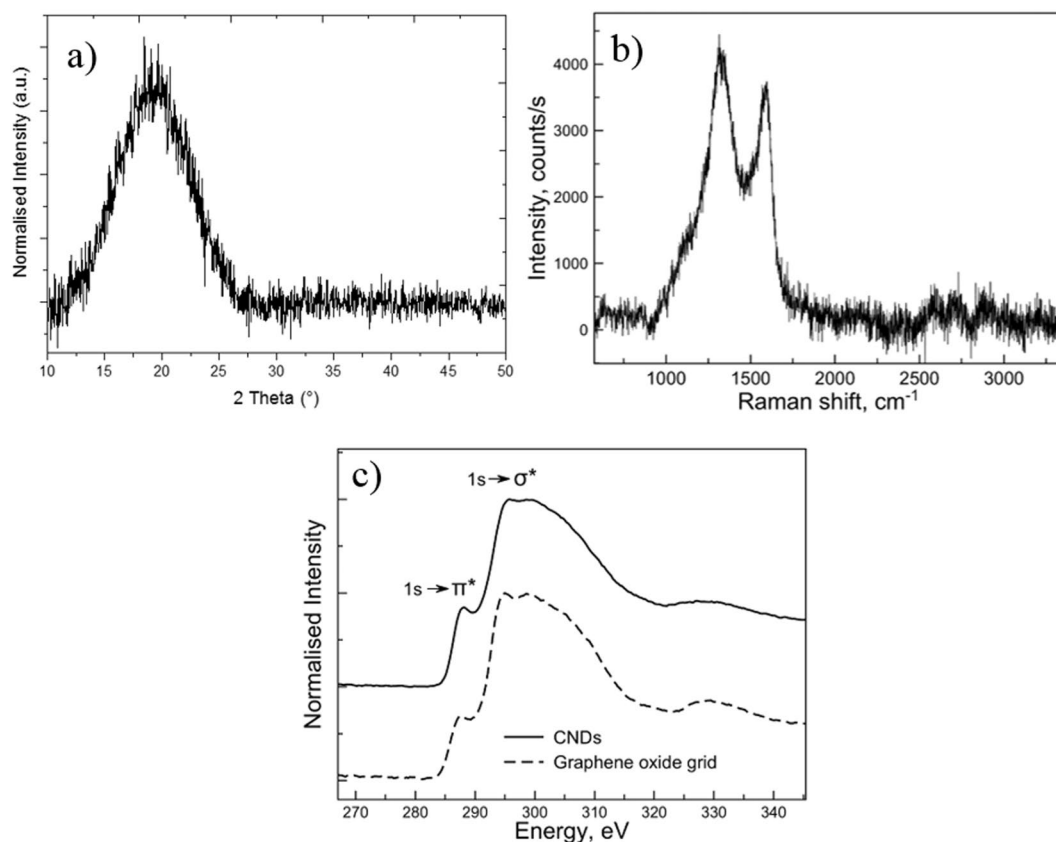


**Figure 2.** Raman (a), XRD (b) and EELS (c) data for glucose CNDs together with the graphene oxide grid reference.

BWF shape to fit G band. We also tested a combination of double Gaussian fitting and Gaussian + BWF, but neither provided an adequate fit to the data.

The Raman data of CNDs indicate that the sample has a significant degree of disorder which is reflected in increased D and G peaks width<sup>45</sup>. D band originates from aromatic conjugated sp<sup>2</sup> six-membered carbon rings<sup>46</sup>,



	D band, Lorentzian [ $\text{cm}^{-1}$ ] Position/FWHM	G band, BWF [ $\text{cm}^{-1}$ ] Position/FWHM
Graphene	—	1586/10 <sup>73</sup>
Graphite	—	1582/12 <sup>74</sup>
Glucose nanodots (size: 5.2 nm)	1322/224	1584/102

**Table 1.** Summary of the analysis of Raman data for all carbon nanodots. Data fitting has been carried out using Lorentzian peaks. The last column shows the ratio of D to G band intensity.

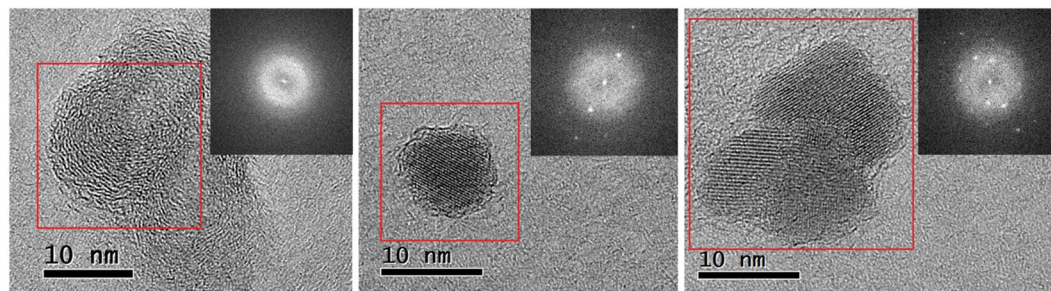


**Figure 3.** TEM micrographs of the glucose-derived CNDs taken at 80 kV showing a number of different crystalline structures: amorphous structure (a), onion-like carbon structure and amorphous crystalline structure (b) crystalline carbon and (c) a mixture of expanded graphite and crystalline carbon. Fast Fourier transforms taken from the red-boxed areas are inset.

hence an increase in D peak intensity reflects large number of such ring clusters. Consequently, broadening of D band reflects disorder in aromatic clusters. Looking at D band peak width information in Table 1, we observe that glucose-derived CNDs show a relatively high level of aromatic ring disorder. The position of the D band strongly depends on excitation energy<sup>47</sup> and for He-Ne (632.8 nm) laser used here the peak is expected at around 1325  $\text{cm}^{-1}$  in graphite. This position is close to the ones observed in our sample, suggesting presence of graphitic structures in our samples. Raman signal (albeit weak) in the region between 2500  $\text{cm}^{-1}$  and 3000  $\text{cm}^{-1}$  provides further evidence for presence of graphite-like structures (see Fig. 1a), as opposed to simply amorphous carbon. Single layer graphene exhibits very strong and narrow 2D peak at around 2700  $\text{cm}^{-1}$ <sup>48</sup>, which is subject to broadening, splitting and reduction of intensity in multi-layered graphite. In our case, the signal in this region is weak, suggesting the presence of disordered multi-layered graphite-like structures.

The observed G band is clearly asymmetric which, on the lower wavelength side of the peak in nanoscale systems, is usually associated with the phonon confinement<sup>49</sup>, thus suggesting that the particle size is sufficiently small for bulk phonon dispersion description to break down. It is worth pointing out, that our glucose CNDs samples show Raman signal very similar to that observed in graphene oxide<sup>50–53</sup>, which may suggest significant contribution of out-of-plane bonding.

The EELS at carbon K edge shows a broad peak at around 285 eV corresponding to 1s- $\pi^*$  transition observed in  $sp^2$  sites in graphite<sup>54</sup>, followed by a broad 1s- $\sigma^*$  peak at around 300 eV corresponding to both  $sp^2$  and  $sp^3$  sites<sup>55</sup>. The weak exciton peak at the onset of the 1s- $\sigma^*$  feature is not observed in amorphous carbon, and further indicates the presence of graphitic bonding<sup>56</sup>. The EELS signal is very similar to that of the graphene oxide reference (Fig. 2c) indicating contribution from both  $sp^2$  and  $sp^3$  bonded carbon. Further comparison with the published EELS<sup>57–59</sup> data allows placing our samples closer to graphene oxide-amorphous carbon side of the amorphous carbon-graphene oxide-graphene sequence.

These findings suggest that although the XRD pattern in Fig. 2a shows a level of disorder similar to that found in amorphous carbons, Raman exhibits sensitivity to significantly more ordered structures. At the same time, EELS yields data that agree with both the XRD and Raman results, suggesting the existence of predominantly amorphous carbon features with small amounts of graphitized samples and crystalline  $sp^3$  nanodiamond-like structures.

In order to further clarify the crystalline structure of the CNDs derived from the hydrothermal carbonization of glucose and to reduce the rate of knock-on damage under illumination by 200 kV electrons, we have acquired HRTEM images at a lower operating voltage of 80 kV. These TEM micrographs are shown in Fig. 3. Even at 80 kV, we observed beam-induced sample crystallization at a dose of 2000 electrons/ $\text{\AA}^2$  over a 30-minute timeframe (see Supplementary AVI file data taken at 0.5, 1, and 5 minute intervals). Major changes can be seen after about two minutes of beam exposure. Therefore, all our TEM images at 80 kV have been acquired well within this 2-minute timeframe.

The 80 kV HRTEM images and corresponding fast Fourier transforms in Fig. 3a–c show a mixture of at least three types of particles: carbon-onion type, crystalline carbon and graphitic like carbon. Fig. 3a shows the typical pattern of carbon onions with distances between neighbouring shells of about 3.5  $\text{\AA}$ . Fig. 3b,c shows a crystalline structure with an interatomic distances of 2.23, 2.33, 2.5 and 2.8  $\text{\AA}$  suggesting a mixture of  $sp^2$  and  $sp^3$  bonded structures possibly covered by an amorphous carbon layer - an effect previously reported for nanodiamonds<sup>60,61</sup>.

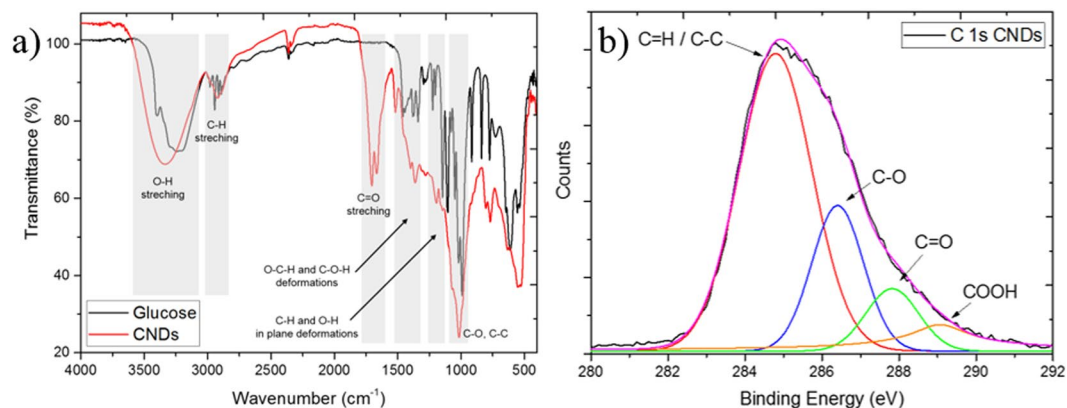


**Figure 4.** FTIR (a) and XPS (b) spectra of glucose-derived CNDs.

We also observe graphitic-like interatomic distance of 3.7 Å corresponding to the (002) of expanded graphite (Fig. 3c). Unlike with the majority of the TEM studies reported in the literature, we observed a heterogeneous structural profile of CNDs, which are subject to further examination in order to understand their exact characteristics.

FTIR and C 1s XPS spectra show indeed the presence of various oxygenated groups on the surface of glucose CNDs. FTIR spectra of glucose-derived carbon nanodots (Fig. 4a) shows the presence of O-H stretching vibrations ( $3600\text{--}3200\text{ cm}^{-1}$ ) along with C=O stretching vibrations at  $1695\text{ cm}^{-1}$ . A combination of O-C-H and C-O-H absorption bands occur in the region of  $1525\text{--}1350\text{ cm}^{-1}$ . In plane C-H and O-H deformation can be observed at  $1170\text{ cm}^{-1}$  and a band of C-O and C-C stretching was assigned from  $1191\text{ cm}^{-1}$  to  $995\text{ cm}^{-1}$ . The bands in the region of  $875\text{--}750\text{ cm}^{-1}$  are assigned to aromatic C-H out of plane bending vibrations<sup>62,63</sup>. The presence of O-H groups and C-O-C linkages were also confirmed in the deconvoluted C 1s spectra of glucose nanodots with the peak at 286.4 eV (Fig. 4b,c and Table S1 for more detailed results).

It is not very clear whether the oxygenated functional groups are directly linked to the surface of the crystalline carbon nanocrystals or if they are located on the surface of the amorphous carbon matrix surrounding each individual fluorescent carbon nanocrystal. Presumably there is a combination of both which explains the expanded graphitic structure observed from electron diffraction (3.7 nm). Nevertheless, XPS and FTIR show that glucose-derived NDs have a high number of polar oxygenated functionalities on their surface consisting of a mixture of hydroxyl, carboxyl and carbonyl functionalities.

Optical properties of CNDs have attracted significant interest with the vast majority of the reports on light emission in CNDs synthesized by HTC route indicate excitation-dependence of the light emission. The detailed excitation-dependent photoluminescence experiments reveal a complex picture of light emission (Fig. S2B and C) with strong emission in the blue-green region of the visible light spectrum. These emission spectra show a change in the shape of the spectra together with the excitation-dependent shift usually observed in photoluminescence (PL) spectra of CNDs suspended in water. This change in the shape is consistent with the structural variations of glucose-derived CNDs observed in TEM (see Fig. 3), indicating an interplay between contribution of various structures seen in TEM to the light emission. Due to the observed complexity of the PL spectral shapes and their excitation-dependence, we produced PL maps to further understand light emission in these systems. From the photoluminescence map (recorded in water suspension) for glucose-derived CNDs (Fig. 5a), we can see that PL spectra show clear dependence on the excitation wavelength, however one can clearly see that this dependence of the PL in water is due to several distinct regions (i.e. 200–290 nm; 290–360 nm and 360–440 nm, see Fig. 5a) where emission is in fact nearly excitation independent, clearly pointing to (and potentially allowing to identify) discrete transition between different emission channels as the excitation wavelength is changed.

The majority of the PL data on CNDs prepared by HTC reported in the literature so far are collected in a colloidal water suspension<sup>16</sup> or in some other solvent, such as ethanol<sup>64</sup> or acetic acid<sup>65</sup>. Solvent polarity is likely to have a strong effect on the surface-related light emission and it has been reported recently<sup>66</sup> that pH can have noticeable effect on the light emission. Thus, in order to further examine origins of the observed excitation-dependent light emission we have collected maps of glucose-derived CNDs (see Fig. 5a–c) in water (relative polarity 1), ethanol (relative polarity 0.654) and hexane (relative polarity 0.009). These data show clear effects of sample-solvent interaction as maps are changing noticeably both above and below 320 nm excitation. In addition to influencing emission, these solvents seem to also noticeably affect the absorption signal in glucose CNDs. (see Fig. S2A). The latter can, of course, reflect the differences in the solubility of the CND subtypes observed in the TEM (Fig. 3). More generally, we have observed strong absorption around 300 nm, which can correspond to the HOMO-LUMO gap, yielding an energy value of the gap of around 4.1 eV. Such value of the HOMO-LUMO gap corresponds to an aromatic structure with only 2–4 rings<sup>67</sup>.

In order to minimize the effect of solvents, the CNDs were freeze-dried and PL was measured using 325 nm and 442 nm laser excitation. Visually, the samples appeared as brownish-layered structures (Fig. S2D) and show bright white light emission (when illuminated by 325 nm laser light) contrary to the blue glow observed in a suspension. The normalized PL data for glucose are shown in Fig. 5d and one can see a significant difference between light emission in suspension and in dry samples. The bright white light emission in dry samples is clearly due to

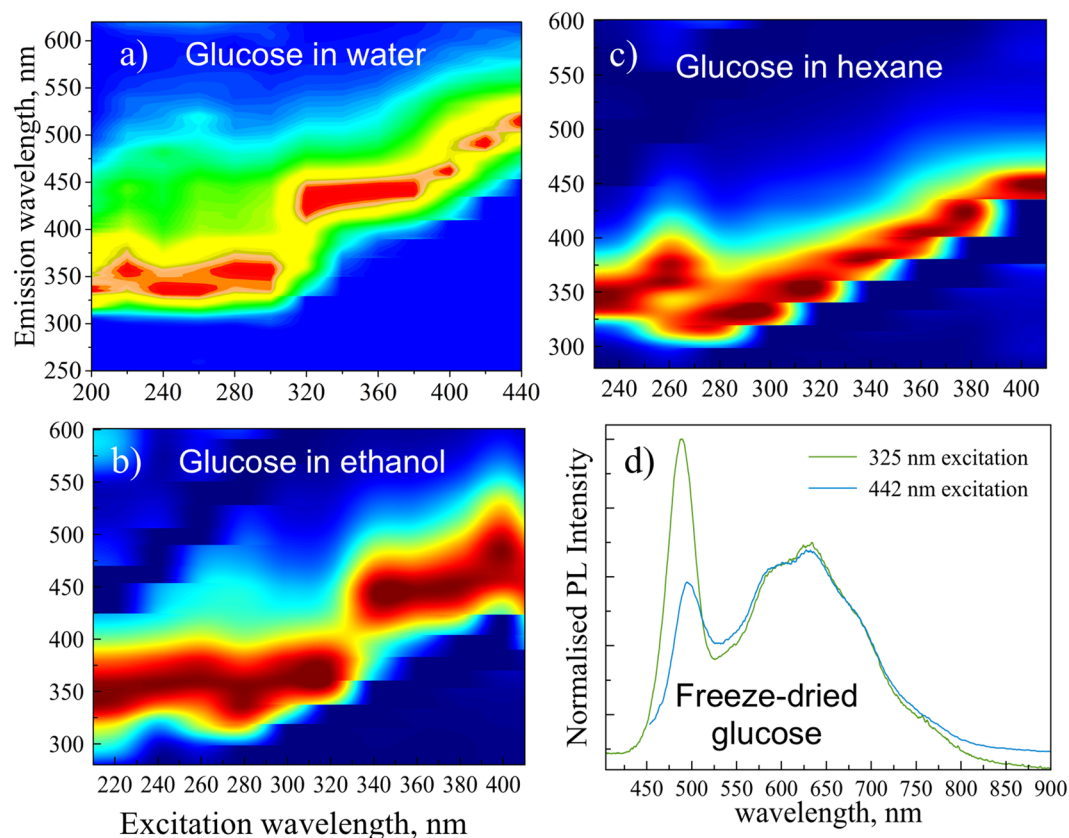


**Figure 5.** PL maps glucose CNDs in water (**a**, relative polarity 1); ethanol (**b**, relative polarity 0.654) and in hexane (**c**, relative polarity 0.009). Normalized PL data of freeze-dried glucose sample with two excitation wavelengths (325 nm and 442 nm) are also shown (**d**).

significant portion of the signal coming from the blue to red region of the spectrum. It is believed that the high abundance in hydroxylic groups on the surface of CNDs, as revealed by the XPS and FTIR studies, assisted in preventing the aggregation induced quenching (AIQ) effect. Furthermore, the peak emission wavelengths shows no dependence on the excitation wavelength. Therefore, we conclude that vast majority of the PL reported to-date for HTC prepared CNDs could be due to particle-solvent interaction, rather than due to CNDs themselves. This conclusion is further corroborated by significant spectral changes (e.g. a narrow PL peak at around 500 nm).

The complex light emission observed in the colloidal suspension of CNDs is in good agreement with the heterogeneous mixture of several types of crystalline carbon phases detected by TEM (Fig. 3) and the diverse nature of functional groups revealed by FTIR and XPS. However, considering the result of TEM analysis, it is rather puzzling that such mild hydrothermal carbonization conditions (200 °C, 30 bars of self-generated pressure) lead to the formation of such defined crystalline structures. As mentioned in the introduction, our group has previously studied the formation mechanism of amorphous hydrothermal carbon spheres and an explanation on the formation mechanism of amorphous HTC spheres is provided in Supplementary Information. Briefly, these form from hydroxymethylfurfural (HMF) which results upon dehydration of glucose via the fructose isomerization. Subsequently HMF polymerizes into small (few nm in size) polymeric nanoclusters, which start growing up to few micrometers in size, and by further dehydration are transformed into hydrothermal carbonaceous spheres<sup>17,68</sup>.

The question arising is how the CND form during this process simultaneous with the HTC microspheres and why they have a crystalline heterogeneous nature. We believe that some of the polymeric nuclei formed initially during the hydrothermal process act as hot spots (due to temperature gradients existing in the autoclave during the HTC process). At the same time, CO/CO<sub>2</sub> gas along with H<sub>2</sub>, are formed *in situ* in the autoclave from partial gasification of glucose under subcritical conditions. These gases deposit onto the hot spot nuclei in a CVD-like process via CO<sub>2</sub> reduction under autogenic pressures (30 bars) leading to the formation of crystalline carbons. We hypothesize that the first crystalline form of carbon CNDs formed under such hydrothermal conditions is *sp*<sup>3</sup>-bonded carbon obtained from amorphous/carbon black type which then can further convert into carbon onions which subsequently form graphitic structures<sup>69</sup>. During incipient stage of glucose transformation via the “hot spots CVD” mechanism mentioned above, a mixture of *sp*<sup>2</sup>/*sp*<sup>3</sup> carbon nanostructures are initially formed which are later converted into predominately *sp*<sup>2</sup> carbon nanostructures<sup>69</sup>. It was also demonstrated<sup>70,71</sup> that the intershell distance in carbon onions from nanodiamond depends on the temperature and pressure, varying from 3.2–3.8 nm. The transformation of nanodiamond into carbon onions has been demonstrated to be reversible under high temperatures and pressures<sup>70,72</sup>. The nanodiamond derived carbon onion further converts into



nanographite (graphitic CNDs) through further annealing<sup>71</sup>. Due to the hydrothermal conditions the resulting crystalline structures are always accompanied by oxygenated functional groups, which explains the expanded graphitic structures. In addition, these crystalline phases in equilibrium are always accompanied by a larger amount of amorphous or polymeric like carbon resulting from HMF polymer clusters aggregation.

## Experimental Section

**Chemicals:** D-(+)-Glucose was purchased from Sigma-Aldrich. Deionized water was used for all the experiments.

**Synthesis Procedure:** D-(+)-Glucose was used as precursors to synthesize the HTC carbon materials. 4% w/v aqueous glucose solution and placed in a Teflon lined, stainless steel autoclave, which underwent hydrothermal treatment at 200 °C for 6 hours. The obtained dark brown liquid phase was centrifuged at 20,000 rpm for 10 min to separate the liquid containing fluorescent carbon nanodots from the solid black precipitate. The liquid phase containing carbon nanodots was then filtered using standard syringe filters. Further, the liquid phase was freeze dried to obtain the final powder of carbon nanodots which was used for further characterization.

**Structural Characterization:** Transmission electron microscopy (TEM) was performed on JEOL JEM-2010 electron microscope operating at 200 kV to observe the morphologies of the samples. Carbon nanodots were dispersed in ethanol and one drop was applied onto the copper grids coated with amorphous carbon for TEM measurements. HRTEM was performed in an image-corrected FEI Titan (S)TEM operated at 80 kV in order to reduce the effects of “*in situ*” graphitization. Electron energy loss spectroscopy (EELS) was performed on JEOL 2100 F FEG-TEM operating at 100 kV equipped with a Gatan Tridiem Filter. Raman spectra were measured using a Renishaw 1000 microspectrometer with excitation wavelength of 633 nm. X-ray diffraction (XRD) patterns were recorded using Panalytical Xpert Pro diffractometer equipped with Ni filtered Cu K $\alpha$  radiation ( $\lambda_1 = 1.5406 \text{ \AA}$  and  $\lambda_2 = 1.5444 \text{ \AA}$ ) collected in the  $2\theta$  range from 5° to 70°. Fourier Transform Infrared Spectroscopy (FTIR) measurements were recorded using a Bruker Tensor 27 instrument equipped with diamond lens Attenuated Total Reflectance (ATR) module in the range from 4000  $\text{cm}^{-1}$  to 400  $\text{cm}^{-1}$ . XPS measurements were carried out on a K-Alpha spectrometer utilizing a monochromatic AlK $\alpha$  X-ray source (1486.6 eV, 400  $\mu\text{m}$  spot size, 36 W).

**Optical Characterization:** The absorption spectra were recorded using the Perkin Elmer Lambda LS 35 UV-visible spectrometer. The fluorescence spectra were recorded using Perkin Elmer LS 55 fluorescence spectrometer. Slit width of 6 nm both for excitation and emission was used when measuring fluorescence emission of aqueous solution of carbon nanodots. The excitation wavelength was increased from 200 nm to 480 nm in 20 nm increments, and the corresponding fluorescence emission spectrum was recorded. Quartz cuvettes (Thor Labs) were used for the measurements of UV-Vis absorption spectra and fluorescence emission spectra. These quartz cuvettes have a 10 mm transmitted path length through the sample and a certified wavelength range from 200–3000 nm. We have chosen quartz cuvettes for UV-Vis absorption and fluorescence emission measurements because of their very good transmission spectra all the way down to 200 nm (78% transmission at 200 nm), while plastic and glass cuvettes show very low transmission below 290 nm and may contribute to the background emission.

## Conclusion

In this paper, we examined the structure and optical properties of CNDs produced from glucose by hydrothermal carbonization. We found that the product of the reaction is a heterogeneous mixture of amorphous-like, carbon-black type and various crystalline nanoparticles including carbon onions and expanded nanographite. We show that even at relatively low electron doses, effects of sample annealing by TEM are observed. We suggested a formation mechanism for these crystalline particles forming under such mild conditions based on HMF polymerization into HTC nuclei followed by formation of hot spots due to temperature gradients and deposition of “*in situ* formed” gases onto these hot spots under pressurized conditions leading to the formation of crystalline particles.

We have further examined light absorption and emission in these systems and found complex excitation-dependent light emission for samples suspended in solvents. We found that this complex emission picture is clearly affected by the polarity of the solvent used to prepare colloidal suspension. Furthermore, we found that solvent-free samples show light emission drastically different from samples in colloidal solution and demonstrate no excitation-dependent light emission.

Thus, this work clearly points to the need for untangling effects of sample phase heterogeneity and surface functionalization on the light emission in HTC-prepared CNDs. This work suggests that future research in HTC-prepared CNDs must focus on resolving the problem of heterogeneity of the final products and ensuring adequate structural characterization using low dose TEM. Further support on the mechanism of formation should be achieved by performing a series of *in situ* measurements based on XRD (both WAXS and SAXS) and neutron scattering studies.

## References

- Zhu, S. *et al.* The photoluminescence mechanism in carbon dots (graphene quantum dots, carbon nanodots, and polymer dots): current state and future perspective. *Nano Research* **8**, 355–381, <https://doi.org/10.1007/s12274-014-0644-3> (2015).
- Sahu, S., Behera, B., Maiti, T. K. & Mohapatra, S. Simple one-step synthesis of highly luminescent carbon dots from orange juice: application as excellent bio-imaging agents. *Chemical communications (Cambridge, England)* **48**, 8835–8837, <https://doi.org/10.1039/c2cc33796g> (2012).
- Yang, Z. C. *et al.* Intrinsically fluorescent carbon dots with tunable emission derived from hydrothermal treatment of glucose in the presence of monopotassium phosphate. *Chemical communications (Cambridge, England)* **47**, 11615–11617, <https://doi.org/10.1039/c1cc14860e> (2011).
- Chandra, S., Das, P., Bag, S., Laha, D. & Pramanik, P. Synthesis, functionalization and bioimaging applications of highly fluorescent carbon nanoparticles. *Nanoscale* **3**, 1533–1540, <https://doi.org/10.1039/c0nr00735h> (2011).
- Mirtchev, P., Henderson, E. J., Soheilnia, N., Yip, C. M. & Ozin, G. A. Solution phase synthesis of carbon quantum dots as sensitizers for nanocrystalline TiO<sub>2</sub> solar cells. *Journal of Materials Chemistry* **22**, 1265–1269 (2012).

6. Zhu, S. *et al.* Highly photoluminescent carbon dots for multicolor patterning, sensors, and bioimaging. *Angewandte Chemie (International ed. in English)* **52**, 3953–3957, <https://doi.org/10.1002/anie.201300519> (2013).
7. Lu, W. *et al.* High-quality water-soluble luminescent carbon dots for multicolor patterning, sensors, and bioimaging. *RSC Adv.* **5**, 16972–16979, <https://doi.org/10.1039/c4ra16233a> (2015).
8. Wang, L. *et al.* Gram-scale synthesis of single-crystalline graphene quantum dots with superior optical properties. *Nat Commun* **5**, 5357, <https://doi.org/10.1038/ncomms6357> (2014).
9. Lai, T. *et al.* Hybrid carbon source for producing nitrogen-doped polymer nanodots: one-pot hydrothermal synthesis, fluorescence enhancement and highly selective detection of Fe(III). *Nanoscale* **5**, 8015–8021, <https://doi.org/10.1039/c3nr02014b> (2013).
10. Liu, S. *et al.* Hydrothermal treatment of grass: a low-cost, green route to nitrogen-doped, carbon-rich, photoluminescent polymer nanodots as an effective fluorescent sensing platform for label-free detection of Cu(II) ions. *Advanced materials (Deerfield Beach, Fla.)* **24**, 2037–2041, <https://doi.org/10.1002/adma.201200164> (2012).
11. Huang, H. *et al.* One-pot green synthesis of nitrogen-doped carbon nanoparticles as fluorescent probes for mercury ions. *RSC Advances* **3**, 21691–21696, <https://doi.org/10.1039/c3ra43452d> (2013).
12. Zhu, S. *et al.* Graphene quantum dots with controllable surface oxidation, tunable fluorescence and up-conversion emission. *RSC Advances* **2**, 2717–2720, <https://doi.org/10.1039/c2ra20182h> (2012).
13. Tao, H. *et al.* *In vivo* NIR fluorescence imaging, biodistribution, and toxicology of photoluminescent carbon dots produced from carbon nanotubes and graphite. *Small* **8**, 281–290, <https://doi.org/10.1002/smll.201101706> (2012).
14. Zhu, S. *et al.* Strongly green-photoluminescent graphene quantum dots for bioimaging applications. *Chemical communications (Cambridge, England)* **47**, 6858–6860, <https://doi.org/10.1039/c1cc11122a> (2011).
15. Zhu, H. *et al.* Microwave synthesis of fluorescent carbon nanoparticles with electrochemiluminescence properties. *Chemical communications (Cambridge, England)*, 5118–5120, <https://doi.org/10.1039/b907612c> (2009).
16. Mehta, V. N., Jha, S., Singhal, R. K. & Kailasa, S. K. Preparation of multicolor emitting carbon dots for HeLa cell imaging. *New J. Chem.* **38**, 6152–6160, <https://doi.org/10.1039/c4nj00840e> (2014).
17. Titirici, M.-M., White, R. J., Falco, C. & Sevilla, M. Black perspectives for a green future: hydrothermal carbons for environment protection and energy storage. *Energy & Environmental Science* **5**, 6796–6822, <https://doi.org/10.1039/c2ee21166a> (2012).
18. Shen, C., Yao, W. & Lu, Y. One-step synthesis of intrinsically functionalized fluorescent carbon nanoparticles by hydrothermal carbonization from different carbon sources. *Journal of Nanoparticle Research* **15**, 2019, <https://doi.org/10.1007/s11051-013-2019-1> (2013).
19. Yang, Y. *et al.* One-step synthesis of amino-functionalized fluorescent carbon nanoparticles by hydrothermal carbonization of chitosan. *Chemical communications (Cambridge, England)* **48**, 380–382, <https://doi.org/10.1039/c1cc15678k> (2012).
20. Ye, R. *et al.* Coal as an abundant source of graphene quantum dots. *Nat Commun* **4**, 2943, <https://doi.org/10.1038/ncomms3943> (2013).
21. Li, H. *et al.* Water-soluble fluorescent carbon quantum dots and photocatalyst design. *Angewandte Chemie (International ed. in English)* **49**, 4430–4434, <https://doi.org/10.1002/anie.200906154> (2010).
22. Hsu, P. C. & Chang, H. T. Synthesis of high-quality carbon nanodots from hydrophilic compounds: role of functional groups. *Chemical communications (Cambridge, England)* **48**, 3984–3986, <https://doi.org/10.1039/c2cc30188a> (2012).
23. Bao, L. *et al.* Electrochemical tuning of luminescent carbon nanodots: from preparation to luminescence mechanism. *Advanced materials (Deerfield Beach, Fla.)* **23**, 5801–5806, <https://doi.org/10.1002/adma.201102866> (2011).
24. Fu, M. *et al.* Carbon Dots: A Unique Fluorescent Cocktail of Polycyclic Aromatic Hydrocarbons. *Nano Lett* **15**, 6030–6035, <https://doi.org/10.1021/acs.nanolett.5b02215> (2015).
25. Demchenko, A. P. & Dekaliuk, M. O. The origin of emissive states of carbon nanoparticles derived from ensemble-averaged and single-molecular studies. *Nanoscale* **8**, 14057–14069, <https://doi.org/10.1039/c6nr02669a> (2016).
26. Sun, Y. P. *et al.* Quantum-sized carbon dots for bright and colorful photoluminescence. *J Am Chem Soc* **128**, 7756–7757, <https://doi.org/10.1021/ja062677d> (2006).
27. Pan, D. *et al.* Observation of pH-, solvent-, spin-, and excitation-dependent blue photoluminescence from carbon nanoparticles. *Chemical communications (Cambridge, England)* **46**, 3681–3683, <https://doi.org/10.1039/c000114g> (2010).
28. Jiang, K. *et al.* Triple-Mode Emission of Carbon Dots: Applications for Advanced Anti-Counterfeiting. *Angewandte Chemie (International ed. in English)* **55**, 7231–7235, <https://doi.org/10.1002/anie.201602445> (2016).
29. Sciortino, A. *et al.* Solvatochromism Unravels the Emission Mechanism of Carbon Nanodots. *J Phys Chem Lett* **7**, 3419–3423, <https://doi.org/10.1021/acs.jpcclett.6b01590> (2016).
30. Reckmeier, C. J., Wang, Y., Zboril, R. & Rogach, A. L. Influence of Doping and Temperature on Solvatochromic Shifts in Optical Spectra of Carbon Dots. *The Journal of Physical Chemistry C* **120**, 10591–10604, <https://doi.org/10.1021/acs.jpcc.5b12294> (2016).
31. Dong, J., Solntsev, K. M. & Tolbert, L. M. Solvatochromism of the green fluorescence protein chromophore and its derivatives. *J Am Chem Soc* **128**, 12038–12039, <https://doi.org/10.1021/ja063128a> (2006).
32. Terenziani, F., Painelli, A., Katan, C., Charlot, M. & Blanchard-Desce, M. Charge instability in quadrupolar chromophores: symmetry breaking and solvatochromism. *J Am Chem Soc* **128**, 15742–15755, <https://doi.org/10.1021/ja064521j> (2006).
33. Chiang, C. L. *et al.* Red-Emitting Fluorenes as Efficient Emitting Hosts for Non-Doped, Organic Red-Light-Emitting Diodes. *Advanced Functional Materials* **15**, 231–238, <https://doi.org/10.1002/adfm.200400102> (2005).
34. Chen, Y. *et al.* A Self-Quenching-Resistant Carbon-Dot Powder with Tunable Solid-State Fluorescence and Construction of Dual-Fluorescence Morphologies for White Light-Emission. *Advanced materials (Deerfield Beach, Fla.)* **28**, 312–318, <https://doi.org/10.1002/adma.201503380> (2016).
35. Hu, Y., Yang, J., Tian, J. & Yu, J.-S. How do nitrogen-doped carbon dots generate from molecular precursors? An investigation of the formation mechanism and a solution-based large-scale synthesis. *Journal of Materials Chemistry B* **3**, 5608–5614, <https://doi.org/10.1039/c5tb01005e> (2015).
36. De, B. & Karak, N. A green and facile approach for the synthesis of water soluble fluorescent carbon dots from banana juice. *RSC Advances* **3**, 8286–8290, <https://doi.org/10.1039/c3ra00088e> (2013).
37. Qu, D. *et al.* Formation mechanism and optimization of highly luminescent N-doped graphene quantum dots. *Sci Rep* **4**, 9, <https://doi.org/10.1038/srep05294> (2014).
38. Xiao, S. J. *et al.* Fluorescent carbon dots: facile synthesis at room temperature and its application for Fe<sup>2+</sup>-sensing. *Journal of Nanoparticle Research* **19**, <https://doi.org/10.1007/s11051-016-3698-1> (2017).
39. Baccile, N. *et al.* Structural Characterization of Hydrothermal Carbon Spheres by Advanced Solid-State MAS13C NMR Investigations. *The Journal of Physical Chemistry C* **113**, 9644–9654, <https://doi.org/10.1021/jp901582x> (2009).
40. Wang, J. *et al.* Large-Scale Green Synthesis of Fluorescent Carbon Nanodots and Their Use in Optics Applications. *Advanced Optical Materials* **3**, 103–111, <https://doi.org/10.1002/adom.201400307> (2015).
41. Zhang, Y. *et al.* Effect of reaction temperature on structure and fluorescence properties of nitrogen-doped carbon dots. *Applied Surface Science* **387**, 1236–1246, <https://doi.org/10.1016/j.apsusc.2016.07.048> (2016).
42. Zhuo, Y., Miao, H., Zhong, D., Zhu, S. & Yang, X. One-step synthesis of high quantum-yield and excitation-independent emission carbon dots for cell imaging. *Materials Letters* **139**, 197–200, <https://doi.org/10.1016/j.matlet.2014.10.048> (2015).
43. Gu, J., Zhang, X., Pang, A. & Yang, J. Facile synthesis and photoluminescence characteristics of blue-emitting nitrogen-doped graphene quantum dots. *Nanotechnology* **27**, 165704, <https://doi.org/10.1088/0957-4484/27/16/165704> (2016).
44. Yoshikawa, M. *et al.* Raman scattering from nanometer-sized diamond. *Applied Physics Letters* **67**, 694–696, <https://doi.org/10.1063/1.115206> (1995).



45. Ferrari, A. C. & Robertson, J. Interpretation of Raman spectra of disordered and amorphous carbon. *Physical Review B* **61**, 14095–14107, <https://doi.org/10.1103/PhysRevB.61.14095> (2000).
46. Castiglioni, C., Negri, F., Rigolio, M. & Zerbi, G. Raman activation in disordered graphites of the A1' symmetry forbidden  $k \neq 0$  phonon: The origin of the D line. *The Journal of Chemical Physics* **115**, 3769–3778, <https://doi.org/10.1063/1.1381529> (2001).
47. Vidano, R. P., Fischbach, D. B., Willis, L. J. & Loehr, T. M. Observation of Raman band shifting with excitation wavelength for carbons and graphites. *Solid State Communications* **39**, 341–344, [https://doi.org/10.1016/0038-1098\(81\)90686-4](https://doi.org/10.1016/0038-1098(81)90686-4) (1981).
48. Ferrari, A. C. & Basko, D. M. Raman spectroscopy as a versatile tool for studying the properties of graphene. *Nat Nanotechnol* **8**, 235–246, <https://doi.org/10.1038/nnano.2013.46> (2013).
49. Campbell, I. H. & Fauchet, P. M. The effects of microcrystal size and shape on the one phonon Raman spectra of crystalline semiconductors. *Solid State Communications* **58**, 739–741, [https://doi.org/10.1016/0038-1098\(86\)90513-2](https://doi.org/10.1016/0038-1098(86)90513-2) (1986).
50. Bo, Z. *et al.* Green preparation of reduced graphene oxide for sensing and energy storage applications. *Sci Rep* **4**, 4684, <https://doi.org/10.1038/srep04684> (2014).
51. Drewniak, S. *et al.* Studies of Reduced Graphene Oxide and Graphite Oxide in the Aspect of Their Possible Application in Gas Sensors. *Sensors (Basel)* **16**, 103, <https://doi.org/10.3390/s16010103> (2016).
52. Kudin, K. N. *et al.* Raman spectra of graphite oxide and functionalized graphene sheets. *Nano Lett* **8**, 36–41, <https://doi.org/10.1021/nl071822y> (2008).
53. Zhang, J. *et al.* Facile synthesis of diverse graphene nanomeshes based on simultaneous regulation of pore size and surface structure. *Sci Rep* **6**, 32310, <https://doi.org/10.1038/srep32310> (2016).
54. Berger, S. D., McKenzie, D. R. & Martin, P. J. EELS analysis of vacuum arc-deposited diamond-like films. *Philosophical Magazine Letters* **57**, 285–290, <https://doi.org/10.1080/09500838808214715> (1988).
55. Fallon, P. J. *et al.* Properties of filtered-ion-beam-deposited diamondlike carbon as a function of ion energy. *Physical Review B* **48**, 4777–4782 (1993).
56. Garvie, L. A. J., Craven, A. J. & Brydson, R. Use of Electron-Energy-Loss near-Edge Fine-Structure in the Study of Minerals. *American Mineralogist* **79**, 411–425 (1994).
57. Andre Mkhoyan, K. *et al.* Atomic and electronic structure of graphene-oxide. *Nano Lett* **9**, 1058–1063, <https://doi.org/10.1021/nl8034256> (2009).
58. Jasinski, J. B. *et al.* Novel graphene oxide/manganese oxide nanocomposites. *RSC Advances* **3**, 22857–22862, <https://doi.org/10.1039/c3ra42254b> (2013).
59. Albert, D. & Michael, F. Substrate-free microwave synthesis of graphene: experimental conditions and hydrocarbon precursors. *New Journal of Physics* **12**, 125013 (2010).
60. Kuznetsov, V. L. *et al.* Study of ultradispersed diamond powders obtained using explosion energy. *Carbon* **29**, 665–668, [https://doi.org/10.1016/0008-6223\(91\)90135-6](https://doi.org/10.1016/0008-6223(91)90135-6) (1991).
61. Tomita, S. *et al.* Diamond nanoparticles to carbon onions transformation: X-ray diffraction studies. *Carbon* **40**, 1469–1474, [https://doi.org/10.1016/s0008-6223\(01\)00311-6](https://doi.org/10.1016/s0008-6223(01)00311-6) (2002).
62. Sevilla, M. & Fuertes, A. B. Chemical and structural properties of carbonaceous products obtained by hydrothermal carbonization of saccharides. *Chemistry* **15**, 4195–4203, <https://doi.org/10.1002/chem.200802097> (2009).
63. Ibrahim, M., Alaam, M., El-Haes, H., Jalbout, A. F. & Leon, A. D. Analysis of the structure and vibrational spectra of glucose and fructose. *Eclética Química* **31**, 15–21 (2006).
64. Bourlino, A. B. *et al.* Surface functionalized carbogenic quantum dots. *Small* **4**, 455–458, <https://doi.org/10.1002/sml.200700578> (2008).
65. Gong, X. *et al.* High-performance liquid chromatographic and mass spectrometric analysis of fluorescent carbon nanodots. *Talanta* **129**, 529–538, <https://doi.org/10.1016/j.talanta.2014.04.008> (2014).
66. Lu, S. *et al.* pH-Dependent Synthesis of Novel Structure-Controllable Polymer-Carbon NanoDots with High Acidophilic Luminescence and Super Carbon Dots Assembly for White Light-Emitting Diodes. *ACS Appl Mater Interfaces* **8**, 4062–4068, <https://doi.org/10.1021/acsami.5b11579> (2016).
67. Eda, G. *et al.* Blue photoluminescence from chemically derived graphene oxide. *Advanced materials (Deerfield Beach, Fla.)* **22**, 505–509, <https://doi.org/10.1002/adma.200901996> (2010).
68. Hu, B. *et al.* Engineering carbon materials from the hydrothermal carbonization process of biomass. *Advanced materials (Deerfield Beach, Fla.)* **22**, 813–828, <https://doi.org/10.1002/adma.200902812> (2010).
69. Hu, S. *et al.* Synthesis and luminescence of nanodiamonds from carbon black. *Materials Science and Engineering: B* **157**, 11–14, <https://doi.org/10.1016/j.mseb.2008.12.001> (2009).
70. Xiao, J., Ouyang, G., Liu, P., Wang, C. X. & Yang, G. W. Reversible nanodiamond-carbon onion phase transformations. *Nano Lett* **14**, 3645–3652, <https://doi.org/10.1021/nl5014234> (2014).
71. Osipov, V. Y. *et al.* Magnetic and high resolution TEM studies of nanographite derived from nanodiamond. *Carbon* **44**, 1225–1234, <https://doi.org/10.1016/j.carbon.2005.10.047> (2006).
72. Barnard, A. S. Theory and modeling of nanocarbon phase stability. *Diamond and Related Materials* **15**, 285–291, <https://doi.org/10.1016/j.diamond.2005.05.007> (2006).
73. Ferrari, A. C. *et al.* Raman spectrum of graphene and graphene layers. *Phys Rev Lett* **97**, 187401, <https://doi.org/10.1103/PhysRevLett.97.187401> (2006).
74. Ferrari, A. C. Raman spectroscopy of graphene and graphite: Disorder, electron–phonon coupling, doping and nonadiabatic effects. *Solid State Communications* **143**, 47–57, <https://doi.org/10.1016/j.ssc.2007.03.052> (2007).

## Acknowledgements

We greatly acknowledge funding by the Materials Research Institute, BBSRC (grant number BB/J001473/1) and an Imperial College Research Fellowship (AEG). X-ray photoelectron spectra was obtained at the National EPSRC XPS Users' Service (NEXUS) at Newcastle University, an EPSRC Mid-Range Facility.

## Author Contributions

N.P. designed the study, carried out experiments and analyzed main data for manuscript submission. N.P., A.M., M.M. and A.S. contributed to manuscript preparation and revision. N.Y. and A.G. performed TEM measurements, M.F. and A.K. performed EELS measurements. All authors reviewed and approved the manuscript.

## Additional Information

**Supplementary information** accompanies this paper at <https://doi.org/10.1038/s41598-018-25012-8>.

**Competing Interests:** The authors declare no competing interests.

**Publisher's note:** Springer Nature remains neutral with regard to jurisdictional claims in published maps and institutional affiliations.



**Open Access** This article is licensed under a Creative Commons Attribution 4.0 International License, which permits use, sharing, adaptation, distribution and reproduction in any medium or format, as long as you give appropriate credit to the original author(s) and the source, provide a link to the Creative Commons license, and indicate if changes were made. The images or other third party material in this article are included in the article's Creative Commons license, unless indicated otherwise in a credit line to the material. If material is not included in the article's Creative Commons license and your intended use is not permitted by statutory regulation or exceeds the permitted use, you will need to obtain permission directly from the copyright holder. To view a copy of this license, visit <http://creativecommons.org/licenses/by/4.0/>.

© The Author(s) 2018